Spontaneous-Symmetry-Breaking Charge Separation Induced by Pseudo-Jahn–Teller Distortion in Organic Photovoltaic Material

Takeaki Zaima,[†,‡] Wataru Ota,[†,‡] Naoki Haruta,[†,‡] Motoyuki Uejima,[¶]
Hideo Ohkita,[§] and Tohru Sato[*,†,‡]

[†]*Fukui Institute for Fundamental Chemistry, Kyoto University, Takano Nishibiraki-cho 34-4, Sakyo-ku, Kyoto 606-8103, Japan*

[‡]*Department of Molecular Engineering, Graduate School of Engineering, Kyoto University, Nishikyo-ku, Kyoto 615-8510, Japan*

[¶]*MOLFEX, Inc., Takano Nishibiraki-cho 34-4, Sakyo-ku, Kyoto 606-8103, Japan*

[§]*Department of Polymer Chemistry, Graduate School of Engineering, Kyoto University, Katsura, Nishikyo-ku, Kyoto 615-8510, Japan*

E-mail: tsato@scl.kyoto-u.ac.jp

Abstract

The driving force of charge separation in the initial photovoltaic conversion process was theoretically investigated using ITIC, non-fullerene acceptor material for organic photovoltaic (OPV) devices, as an example. The density functional theory (DFT) calculations show that the pseudo-Jahn–Teller (PJT) distortion of the S_1 excimer state induces spontaneous-symmetry-breaking charge separation (SSB-CS) between the identical ITIC molecules to give an intermolecular charge-transfer (ICT) excited state, even without the asymmetry of the surrounding environment. The strong PJT effect arises

https://doi.org/10.26434/chemrxiv-2023-tnz5z **ORCID:** https://orcid.org/0000-0002-8044-487X

from the vibronic coupling between the pseudo-degenerate S_1 and S_2 excited states with different irreducible representations (irreps), i.e., A_u for S_1 and A_g for S_2, via the asymmetric vibrational mode with A_u irrep. The vibrational mode responsible for the spontaneous polarization, opposite in one ITIC monomer and the other, is the intramolecular C-C stretching vibration between the core IT and terminal IC units at the stacked region. These results suggest that controlling the PJT effect of the excited states can influence the charge separation efficiency in the initial photovoltaic conversion process.

Organic photovoltaics (OPV) is a photovoltaic conversion system using organic molecules.[1–4] The active layer of an OPV device typically consists of donor and acceptor materials to inhibit carrier recombination at the donor-acceptor interface.[5–7] The photovoltaic conversion process can be divided into the following steps:[8–10] (i) photon absorption creates an exciton in the donor or acceptor regions, (ii) the exciton diffuses to the donor-acceptor interface, (iii) a charge-transfer (CT) state forms, and (iv) free carriers are generated by overcoming the Coulomb attraction between the electron-hole pair. The driving force of the free carrier generation has been considered as an energy offset defined by the HOMO or LUMO energy differences between the donor and acceptor materials.[8] The threshold of the energy offset required to overcome the Coulomb attraction was estimated to be around 0.3 eV.[11,12] However, OPV devices with energy offsets less than 0.3 eV have been recently reported to achieve high power conversion efficiencies (PCEs).[13–20] The driving force of the charge separation in the OPV devices remains unclear, although several contributing factors have been proposed, such as entropy,[21,22] cascade energy landscape,[23–25] and electron delocalization.[26] Symmetry-breaking charge separation (SB-CS), causing the intra- or inter-molecular charge separation between identical fragments, can also be an initial charge separation step in small offset systems.[27–29] In general, the origin of the SB-CS, primarily studied in polar solvents, is attributed to the asymmetry of the surrounding environment, such as solvent coordinates.[30,31]

It has been reported that SB-CS competes with excimer formation.[32,33] An excimer state is defined by an excited state where the electronic wavefunction is symmetrically delocalized over a dimer; that is, an admixture of molecular exciton and charge resonance states.[34–37] A vertical excitation is likely to form an excimer state in the aggregation phase because of the proximity of molecules.[38] The electronic structure of the excimer is pseudo-degenerate. In this case, spontaneous symmetry-breaking during vibrational relaxation can generate an intermolecular CT (ICT) excited state or a locally excited (LE) state from the excimer state (Fig. 1). This symmetry lowering without the surrounding asymmetry is called pseudo-Jahn–Teller (PJT) distortion.[39,40] The strength of the PJT effect, determining whether the adiabatic state becomes an excimer state or an ICT state, depends on the vibronic coupling and energy gap between the pseudo-degenerate electronic states.[39,40]

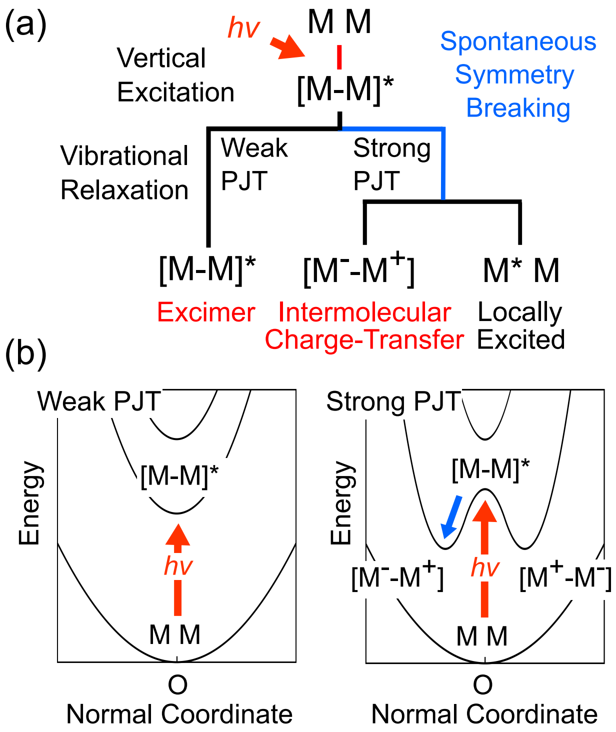

Figure 1: (a) Possible excited electronic states of the dimer after the vibrational relaxation. (b) Schematic representations of the potential energy surfaces with the weak and strong PJT effect.

Based on density functional theory (DFT) calculations, we investigate the driving force of charge separation in the initial photovoltaic conversion process, focusing on the PJT distortion to cause spontaneous symmetry-breaking. The origin of vibronic coupling responsible for the PJT distortion is discussed by its density form, i.e., vibronic coupling density (VCD).[41–43] The non-fullerene acceptor material for OPV devices, ITIC (2,2'-[[6,6,12,12-tetrakis(4-hexylphenyl)-6,12-dihydrodithieno[2,3-d:2',3'-d']-s-indaceno[1,2-b:5,6-b']dithiophene-2,8-diyl]-bis[methylidyne(3-oxo-1H-indene2,1(3H)-diylidene)]]bis[propanedinitrile], Fig. 2 (a)), is used as an illustrative example. The ITIC consists of the core IT (indacenodithieno[3,2-b]thiophene) unit and terminal IC (1,1-dicyanomethylene3-indanone) unit. The absorption spectral lineshape of the ITIC neat film differs from that of the $CHCl_3$ solution;[44] the spectrum in the neat film is red-shifted and broadened compared with that in the solution. This result suggests that ITIC has delocalized wavefunctions in the neat film.

The theory of the PJT effect is briefly described. A molecular system with M nuclei and N electrons is considered. Sets of electronic and mass-weighted normal coordinates are denoted by $\mathbf{r} = (\mathbf{r}_1, \cdots, \mathbf{r}_i, \cdots, \mathbf{r}_N)$ and $\mathbf{Q} = (Q_1, \cdots, Q_\alpha, \cdots, Q_{3M-5 \text{ or } 3M-6})$, respectively. Using the Herzberg–Teller expansion, electronic Hamiltonian, $\hat{H}_e(\mathbf{r}, \mathbf{Q})$, is expanded in terms of the mass-weighted normal coordinates around reference nuclear configuration (the geometry of the saddle point) $\mathbf{Q} = \mathbf{0}$,[45,46]

$$\hat{H}_e(\mathbf{r}, \mathbf{Q}) = \hat{H}_e(\mathbf{r}, \mathbf{0}) + \sum_\alpha \hat{V}_\alpha Q_\alpha + \frac{1}{2} \sum_{\alpha\beta} \hat{W}_{\alpha\beta} Q_\alpha Q_\beta + \cdots, \tag{1}$$

where $\hat{V}_\alpha$ and $\hat{W}_{\alpha\beta}$ are the electronic parts of linear and quadratic vibronic coupling operators,

$$\hat{V}_\alpha = \left(\frac{\partial \hat{H}_e(\mathbf{r}, \mathbf{Q})}{\partial Q_\alpha} \right)_{\mathbf{0}}, \tag{2}$$

$$\hat{W}_{\alpha\beta} = \left(\frac{\partial^2 \hat{H}_e(\mathbf{r}, \mathbf{Q})}{\partial Q_\alpha \partial Q_\beta} \right)_{\mathbf{0}}. \tag{3}$$

Linear vibronic coupling constant (VCC), $V_{nm,\alpha}$, and quadratic VCC, $W_{nm,\alpha\beta}$, between electronic states $|\Psi_m(\mathbf{r}, \mathbf{0})\rangle$ and $|\Psi_n(\mathbf{r}, \mathbf{0})\rangle$, which are the eigenstates of $\hat{H}_e(\mathbf{r}, \mathbf{0})$, are expressed

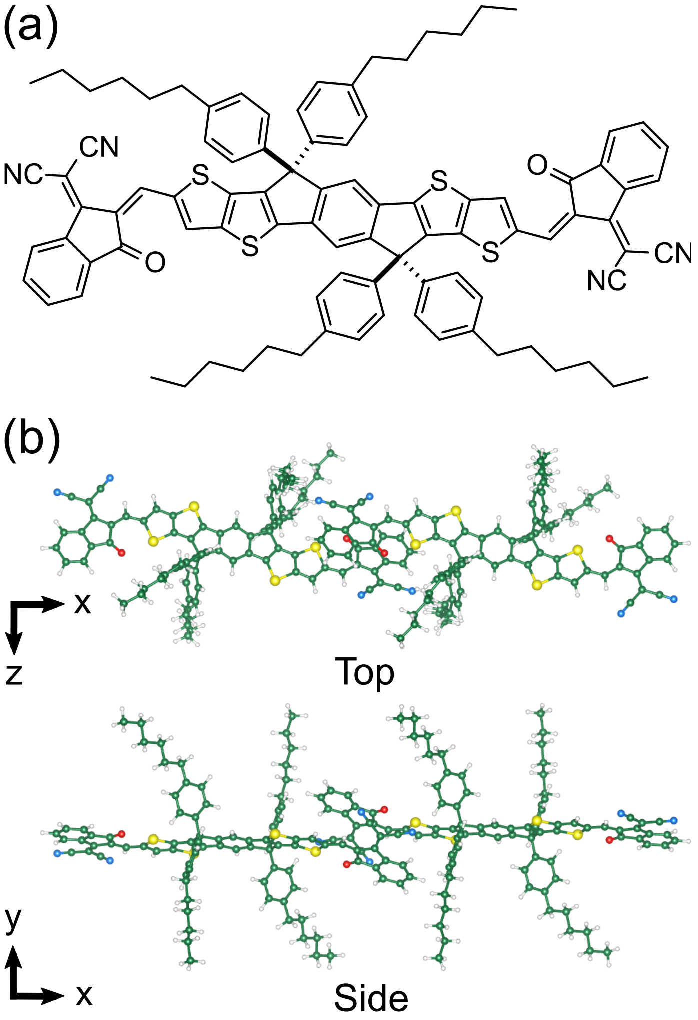

Figure 2: (a) Structure of ITIC. (b) The ITIC dimer with an edge-stacking structure as a computational model in the aggregation phase.

as[45,46]

$$V_{nm,\alpha} = \left\langle \Psi_n(\mathbf{r},\mathbf{0}) \left| \hat{V}_\alpha \right| \Psi_m(\mathbf{r},\mathbf{0}) \right\rangle, \tag{4}$$

$$W_{nm,\alpha\beta} = \left\langle \Psi_n(\mathbf{r},\mathbf{0}) \left| \hat{W}_{\alpha\beta} \right| \Psi_m(\mathbf{r},\mathbf{0}) \right\rangle. \tag{5}$$

Note that $V_{nm,\alpha}$ is non-vanishing when the direct product of the irreducible representation (irrep) for electronic states n and m contains the irrep of vibrational mode α, i.e., $\Gamma_\alpha \in \Gamma_n \otimes \Gamma_m$.[39] Based on the second-order perturbation theory, the energy of electronic state m

along single vibrational mode α is given by[39]

$$E_m(\mathbf{Q}) = E_m(\mathbf{0}) + \frac{1}{2}(W_{m,\alpha} - 2K_{m,\alpha})Q_\alpha^2. \tag{6}$$

In Eq. (6), $W_{m,\alpha} := W_{mm,\alpha\alpha}$ (≥ 0) is the diagonal quadratic VCC and

$$K_{m,\alpha} = \sum_{n \neq m} K_{nm,\alpha}, \tag{7}$$

$$K_{nm,\alpha} = \frac{|V_{nm,\alpha}|^2}{E_n(\mathbf{0}) - E_m(\mathbf{0})}. \tag{8}$$

Large off-diagonal VCC, $|V_{nm,\alpha}|^2$, and small positive energy gap, $E_n(\mathbf{0}) - E_m(\mathbf{0})$, between electronic states n and m give large positive $K_{nm,\alpha}$. When $W_{m,\alpha} - 2K_{m,\alpha} < 0$ in the second term of Eq. (6), electronic state m becomes unstable along vibrational mode α because of the negative curvature of the potential energy surface, which is called the PJT distortion (strong PJT effect).[39,40] Negative $K_{nm,\alpha}$, or negative $E_n(\mathbf{0}) - E_m(\mathbf{0})$, contributes to stabilizing the potential energy surface. The PJT distortion, for example, is known to be the origin of ferroelectricity, i.e., the spontaneous polarization of the crystal.[47,48]

The spatial distribution of VCC can be expressed by VCD;[41–43]

$$V_{nm,\alpha} = \int d\boldsymbol{x}\ \eta_{nm,\alpha}(\boldsymbol{x}), \tag{9}$$

where $\boldsymbol{x} = (x, y, z)$ is the three-dimensional coordinate. Off-diagonal VCD, $\eta_{nm,\alpha}(\boldsymbol{x})$, with $n \neq m$ is defined by

$$\eta_{nm,\alpha}(\boldsymbol{x}) = \rho_{nm}(\boldsymbol{x}) \times v_\alpha(\boldsymbol{x}), \tag{10}$$

where $\rho_{nm}(\boldsymbol{x})$ is the overlap density between electronic states n and m, and $v_\alpha(\boldsymbol{x})$ is the potential derivative of vibrational mode α (for details, see Sec. S1 in the Supporting Information). The VCD enables us to elucidate the origin of vibronic coupling from electronic and vibrational structures separately. The integration of the overlap density and off-diagonal

VCD over the Wigner–Seitz cell give their atomic contributions.[49]

The ground and excited electronic structures of ITIC were computed at the B3LYP/3-21G and TD-B3LYP/3-21G levels of theory, respectively. For the calculations in the $CHCl_3$ solution, the solvent effect was included through the polarizable continuum model (PCM).[50] The S_0 and S_1 optimized structures were confirmed stable by vibrational analysis. The electronic and vibrational structures were computed using Gaussian 16.[51] The absorption spectrum (see Sec. S1.2 for theoretical details), VCC, and VCD were computed using our codes.

First, the electronic structures of the single ITIC molecule in the $CHCl_3$ solution were calculated to check the reliability of the present computational method. The electric dipole transition from S_0 to S_1 is symmetry allowed (Table S1). The calculated S_1 absorption spectrum using the B3LYP functional, compared with the M06-2X and ωB97X-D functionals, reproduces the lineshape and wavelength of the experimental spectrum well (Fig. S1).[44] Hence, the B3LYP functional is considered reasonable. S_1 of the single ITIC molecule has only weak intramolecular CT character from the core IT to terminal IC units both in the vertical excited and adiabatic states (Fig. S2).

Next, the electronic structures of the ITIC dimer in the aggregation phase were calculated. The dimer model was constructed to have an edge-stacking structure (Fig. 2 (b)) because ITIC has been considered packed through the terminal π-π stacking in previous studies.[52–54] The S_0 state of the ITIC dimer is optimized within C_i symmetry. The Franck–Condon S_1 state with the A_u irrep has a large oscillator strength (Table S2). In addition, the electron density difference between S_1 and S_0 is symmetrically delocalized over the ITIC dimer (Fig. 3 (a)), suggesting that vertical excitation generates the S_1 excimer state. Therefore, this excimer state was geometrically optimized. As a result, the symmetry of the S_1 optimized structure is lowered to C_1, indicating that spontaneous symmetry-breaking occurs during the vibrational relaxation. The electron density difference between S_1 and S_0 shows that the adiabatic S_1 state is the ICT excited state having polarization (Fig. 3 (b)).

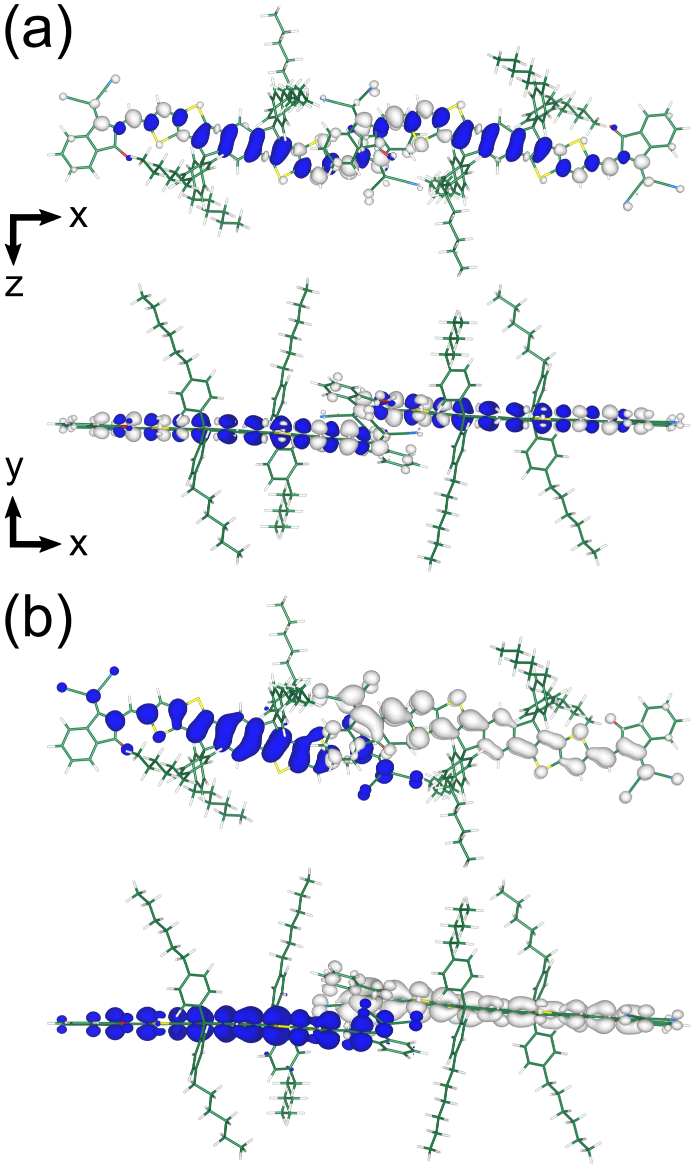

Figure 3: Electron density differences between S_1 and S_0 at the (a) S_0 and (b) S_1 optimized structures for the ITIC dimer. The white/blue region is positive/negative. The isosurface values are 4×10^{-4} a.u.

To investigate the contributing factors of spontaneous symmetry-breaking, the S_1 saddle point was obtained by optimizing the S_1 geometry with C_i symmetry kept. One vibrational mode with imaginary frequency ($924.6i$ cm^{-1}) was obtained at the S_1 saddle point (Fig. 4 (a)). This mode belongs to the A_u irrep lowering the symmetry from C_i to C_1; that is, the direction of the vibrational mode is opposite in one ITIC monomer and the other. The symmetry is lowered by the intramolecular C-C stretching vibration between the core IT and terminal IC units at the stacked region (not the intermolecular vibration). The potential energy surfaces were calculated along the imaginary vibrational mode from the S_1 saddle point (Fig. S3), having double wells characteristic of the PJT distortion.

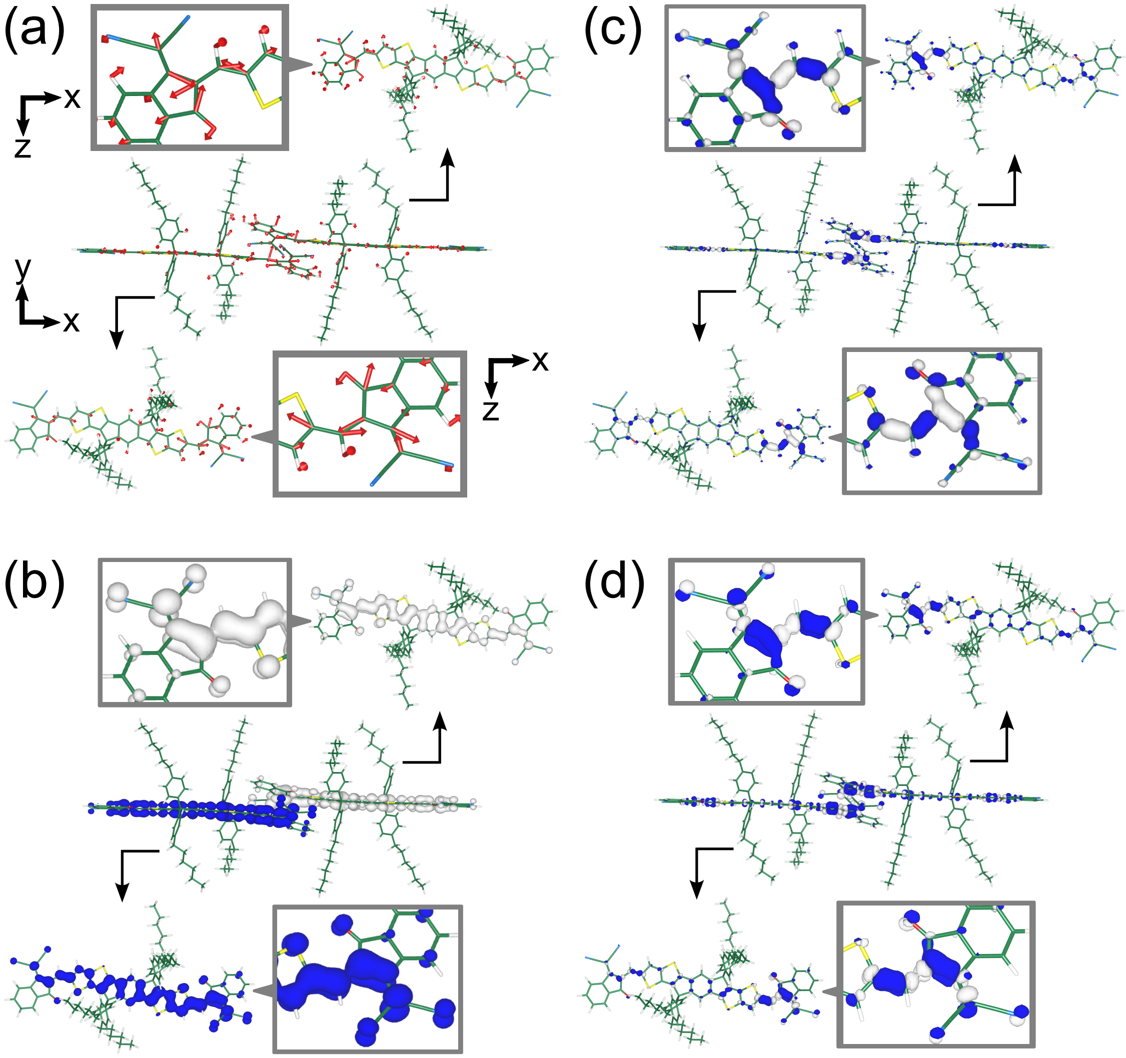

Figure 4: (a) Vibrational mode with the imaginary frequency of $924.6i$ cm^{-1} belonging to the A_u irrep. (b) Overlap density between the pseudo-degenerate S_1 and S_2 states, ρ_{nm}, (c) potential derivative for the imaginary vibrational mode, v_α, and (d) off-diagonal VCD, $\eta_{nm,\alpha}$, at the S_1 saddle point. The direction of the vibrational mode is taken so that the off-diagonal VCC is negative. The white/blue region is positive/negative. The isosurface values of (b), (c), and (d) are 4×10^{-4}, 5×10^{-3}, and 2×10^{-6} a.u., respectively.

Table 1 lists the off-diagonal VCCs between S_1 and other singlets for the imaginary vibrational mode at the S_1 saddle point. Since both the irreps of S_1 and imaginary vibrational mode are the A_u irrep, S_1 couples to the singlets with the A_g irrep because of the selection rule of vibronic coupling. In particular, the off-diagonal VCC between the energetically-close S_1 and S_2 is large. As a result, the square of the off-diagonal VCC divided by the electronic energy difference (Eq. (8)) is significant between these pseudo-degenerate states, primarily contributing to the PJT distortion.

Table 1: Off-diagonal VCC between S_m ($m = 1$) and S_n ($n = 0, 2 - 6$) for imaginary vibrational mode α, $V_{nm,\alpha}$, electronic energy difference between S_m and S_n, $E_n(\mathbf{0}) - E_m(\mathbf{0})$, and square of the off-diagonal VCC divided by the electronic energy difference, $K_{nm,\alpha}$, at the S_1 saddle point (Eq. (8)).

State n	$\lvert V_{nm,\alpha}\rvert$ $/10^{-4}$ a.u.	$E_n - E_m$ /meV	$K_{nm,\alpha}$ $/10^{-5}$ a.u.
$S_0(A_g)$	1.002	-1692	0.000
$S_2(A_g)$	4.092	107	4.258
$S_3(A_g)$	0.012	204	0.000
$S_4(A_u)$	0.000	205	0.000
$S_5(A_u)$	0.000	443	0.000
$S_6(A_g)$	0.559	452	0.019

The off-diagonal VCD analysis was performed to elucidate the origin of the large vibronic coupling responsible for the PJT distortion. Figs. 4 (b)-(d) show the results of the off-diagonal VCD analysis between the pseudo-degenerate S_1 and S_2 states for the imaginary vibrational mode. The overlap density between S_1 and S_2 has a large distribution at the stacked region (see Fig. S4 for the atomic decomposition), coupling to the potential derivative of the vibrational mode localized there. As a result, the off-diagonal VCD is large at the C-C bonds between the core IT and terminal IC units at the stacked region (Fig. S4). The overlap density has different signs between the ITIC monomers. This characteristic distribution is related to the major configurations of the S_1 and S_2 excimer states, as discussed below.

The adiabatic S_1 state of the ITIC dimer becomes the ICT state rather than the LE state after the PJT distortion. The reason is investigated based on the electron configuration of the excimer states at the S_1 saddle point. Using the electron configurations represented by the ITIC monomer orbitals, the S_1 to S_4 states within C_i symmetry can be approximately expressed as (Fig. 5; see Sec. S3.1 for the derivations)

$$\begin{aligned}
|\mathrm{S}_1\rangle &\approx \frac{1}{2}\left[(|\Phi_{\mathrm{HO},L}^{\mathrm{LU},L}\rangle - |\Phi_{\mathrm{HO},R}^{\mathrm{LU},R}\rangle) - (|\Phi_{\mathrm{HO},R}^{\mathrm{LU},L}\rangle - |\Phi_{\mathrm{HO},L}^{\mathrm{LU},R}\rangle)\right], && (11)\\
|\mathrm{S}_2\rangle &\approx \frac{1}{\sqrt{2}}(|\Phi_{\mathrm{HO},R}^{\mathrm{LU},L}\rangle + |\Phi_{\mathrm{HO},L}^{\mathrm{LU},R}\rangle), && (12)\\
|\mathrm{S}_3\rangle &\approx \frac{1}{\sqrt{2}}(|\Phi_{\mathrm{HO},L}^{\mathrm{LU},L}\rangle + |\Phi_{\mathrm{HO},R}^{\mathrm{LU},R}\rangle), && (13)\\
|\mathrm{S}_4\rangle &\approx \frac{1}{2}\left[(|\Phi_{\mathrm{HO},L}^{\mathrm{LU},L}\rangle - |\Phi_{\mathrm{HO},R}^{\mathrm{LU},R}\rangle) + (|\Phi_{\mathrm{HO},R}^{\mathrm{LU},L}\rangle - |\Phi_{\mathrm{HO},L}^{\mathrm{LU},R}\rangle)\right], && (14)
\end{aligned}$$

where $|\Phi_{\mathrm{HO},L/R}^{\mathrm{LU},L/R}\rangle$ represents the electron configuration of a single-electron excitation from the HOMO to LUMO of the left (L) and right (R) ITIC monomers. S_1 and S_4 are the equal admixtures of the molecular exciton and charge resonance states. S_2 is the charge resonance state, whereas S_3 is the molecular exciton state. Since S_2 is the charge resonance state, the PJT distortion arising from the vibronic coupling between S_1 and S_2 induces the ICT excited state. Tables S4 and S5 summarize the overlap densities between the pseudo-degenerate electronic states. In particular, the overlap density between S_1 and S_2 is given by

$$\rho_{21} \approx \frac{1}{2\sqrt{2}}\left[-(|\phi_{\mathrm{HO}}^{L}|^2 + |\phi_{\mathrm{LU}}^{L}|^2) + (|\phi_{\mathrm{HO}}^{R}|^2 + |\phi_{\mathrm{LU}}^{R}|^2)\right] \qquad (15)$$

where $\phi_{\mathrm{HO/LU}}^{L/R}$ represents the monomer orbital. The left/right monomer orbitals are obtained by inverting the right/left monomer orbitals, $i : \phi^{L/R} \mapsto \phi^{R/L}$ (Fig. S5). ρ_{21} is negative on the left monomer and positive on the right monomer. The non-canceling overlap density contributes to the large off-diagonal VCC between S_1 and S_2. The characteristic electronic structures emerge because of pseudo-degeneracy.[38,55]

Finally, the electronic structures of the ITIC dimer were calculated considering the packing effect in the aggregation phase to ensure the validity of the above computational model. The aggregated structure was modeled using CONFLEX 9 (Fig. S6 (a)).[56] The electronic structures were computed based on the ONIOM approach,[57] where the central dimer was treated as a quantum mechanics (QM) region and the surrounding 30 molecules were treated

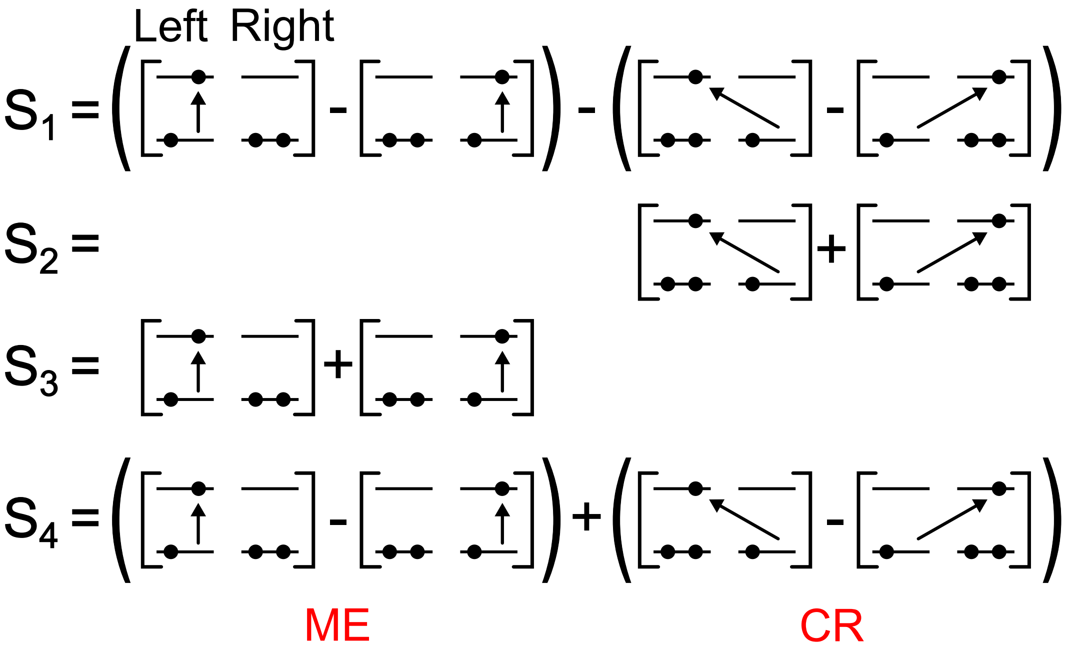

Figure 5: Electron configurations of the ITIC dimer at the S_1 saddle point with C_i symmetry. ME and CR represent the molecular exciton and charge resonance configurations, respectively.

as a molecular mechanics (MM) region (Fig. S6 (b)). The MM region was fixed during the geometry optimization of the QM region. The adiabatic S_1 state of the ITIC dimer has the ICT character, even considering the packing effect (Fig. S7).

In summary, we found that the PJT distortion induces the spontaneous SB-CS (SSB-CS) between the identical ITIC molecules attributed to the vibronic coupling between the pseudo-degenerate S_1 and S_2 states having the significant charge resonance configuration. The vibrational mode responsible for the symmetry lowering, asymmetric in one ITIC monomer and the other, is the intramolecular C-C stretching vibration between the core IT and terminal IC units at the stacked region. It should be emphasized that SB-CS originating from the PJT distortion can occur in either intermolecular or intramolecular interactions without the asymmetry of the surrounding environment. The degree of stabilization by symmetry-breaking depends on the vibronic coupling and energy gap between the pseudo-degenerate electronic states (although the reorganization of the surrounding environment accompanied by symmetry-breaking may enhance stabilizing the system), which can affect the charge separation efficiency in the initial photovoltaic conversion process.

Acknowledgement

This study was partly supported by JSPS KAKENHI Grant Numbers JP22H02157 in Scientific Research (B) (T.S.), JP22K05253 in Scientific Research (C) (T.S.), JP21H04692 in Scientific Research (A) (H.O.), and JP22K19062 in Challenging Research (Exploratory) (H.O.). T.Z. acknowledges the support from JST SPRING, Grant Number JPMJSP2110. Numerical calculations were partly performed using Supercomputer System, Institute for Chemical Research, Kyoto University, Academic Center for Computing and Media Studies (ACCMS), Kyoto University, the information initiative center, Hokkaido University, and Research Center for Computational Science, Okazaki (Project: 22-IMS-C065).

Supporting Information Available

Theoretical details and additional computational results.

References

(1) Günes, S.; Neugebauer, H.; Sariciftci, N. S. Conjugated Polymer-Based Organic Solar Cells. *Chem. Rev.* **2007**, *107*, 1324–1338.

(2) Kippelen, B.; Brédas, J.-L. Organic Photovoltaics. *Energy Environ. Sci.* **2009**, *2*, 251–261.

(3) Heeger, A. J. 25th Anniversary Article: Bulk Heterojunction Solar Cells: Understanding the Mechanism of Operation. *Adv. Mater.* **2014**, *26*, 10–28.

(4) Inganäs, O. Organic Photovoltaics Over Three Decades. *Adv. Mater.* **2018**, *30*, 1800388.

(5) Hiramoto, M.; Fujiwara, H.; Yokoyama, M. Three-Layered Organic Solar Cell with a Photoactive Interlayer of Codeposited Pigments. *Appl. Phys. Lett.* **1991**, *58*, 1062–1064.

(6) Yu, G.; Gao, J.; Hummelen, J. C.; Wudl, F.; Heeger, A. J. Polymer Photovoltaic Cells: Enhanced Efficiencies via a Network of Internal Donor-Acceptor Heterojunctions. *Science* **1995**, *270*, 1789–1791.

(7) Halls, J.; Walsh, C.; Greenham, N. C.; Marseglia, E.; Friend, R. H.; Moratti, S.; Holmes, A. Efficient Photodiodes from Interpenetrating Polymer Networks. *Nature* **1995**, *376*, 498–500.

(8) Peumans, P.; Yakimov, A.; Forrest, S. R. Small Molecular Weight Organic Thin-Film Photodetectors and Solar Cells. *J. Appl. Phys.* **2003**, *93*, 3693–3723.

(9) Brédas, J.-L.; Norton, J. E.; Cornil, J.; Coropceanu, V. Molecular Understanding of Organic Solar Cells: The Challenges. *Acc. Chem. Res.* **2009**, *42*, 1691–1699.

(10) Clarke, T. M.; Durrant, J. R. Charge Photogeneration in Organic Solar Cells. *Chem. Rev.* **2010**, *110*, 6736–6767.

(11) Scharber, M. C.; Mühlbacher, D.; Koppe, M.; Denk, P.; Waldauf, C.; Heeger, A. J.; Brabec, C. J. Design Rules for Donors in Bulk-Heterojunction Solar Cells—Towards 10% Energy-Conversion Efficiency. *Adv. Mater.* **2006**, *18*, 789–794.

(12) Janssen, R. A.; Nelson, J. Factors Limiting Device Efficiency in Organic Photovoltaics. *Adv. Mater.* **2013**, *25*, 1847–1858.

(13) Kawashima, K.; Tamai, Y.; Ohkita, H.; Osaka, I.; Takimiya, K. High-Efficiency Polymer Solar Cells with Small Photon Energy Loss. *Nat. Commun.* **2015**, *6*, 1–9.

(14) Lin, Y.; Wang, J.; Zhang, Z.-G.; Bai, H.; Li, Y.; Zhu, D.; Zhan, X. An Electron Acceptor Challenging Fullerenes for Efficient Polymer Solar Cells. *Adv. Mater.* **2015**, *27*, 1170–1174.

(15) Zhao, W.; Qian, D.; Zhang, S.; Li, S.; Inganäs, O.; Gao, F.; Hou, J. Fullerene-Free Polymer Solar Cells with over 11% Efficiency and Excellent Thermal Stability. *Adv. Mater.* **2016**, *28*, 4734–4739.

(16) Baran, D.; Kirchartz, T.; Wheeler, S.; Dimitrov, S.; Abdelsamie, M.; Gorman, J.; Ashraf, R. S.; Holliday, S.; Wadsworth, A.; Gasparini, N., et al. Reduced Voltage Losses Yield 10% Efficient Fullerene Free Organic Solar Cells with > 1 V Open Circuit Voltages. *Energy Environ. Sci.* **2016**, *9*, 3783–3793.

(17) Chen, S.; Wang, Y.; Zhang, L.; Zhao, J.; Chen, Y.; Zhu, D.; Yao, H.; Zhang, G.; Ma, W.; Friend, R. H.; Chow, P. C. Y.; Gao, F.; Yan, H. Efficient Nonfullerene Organic Solar Cells with Small Driving Forces for Both Hole and Electron Transfer. *Adv. Mater.* **2018**, *30*, 1804215.

(18) Li, S.; Zhan, L.; Sun, C.; Zhu, H.; Zhou, G.; Yang, W.; Shi, M.; Li, C.-Z.; Hou, J.; Li, Y.; Chen, H. Highly Efficient Fullerene-Free Organic Solar Cells Operate at Near Zero Highest Occupied Molecular Orbital Offsets. *J. Am. Chem. Soc.* **2019**, *141*, 3073–3082.

(19) Yuan, J.; Zhang, Y.; Zhou, L.; Zhang, G.; Yip, H.-L.; Lau, T.-K.; Lu, X.; Zhu, C.; Peng, H.; Johnson, P. A.; Leclerc, M.; Cao, Y.; Ulanski, J.; Li, Y.; Zou, Y. Single-Junction Organic Solar Cell with Over 15% Efficiency Using Fused-Ring Acceptor with Electron-Deficient Core. *Joule* **2019**, *3*, 1140–1151.

(20) Sun, C.; Qin, S.; Wang, R.; Chen, S.; Pan, F.; Qiu, B.; Shang, Z.; Meng, L.; Zhang, C.; Xiao, M.; Yang, C.; Li, Y. High Efficiency Polymer Solar Cells with Efficient Hole Transfer at Zero Highest Occupied Molecular Orbital Offset between Methylated Polymer Donor and Brominated Acceptor. *J. Am. Chem. Soc.* **2020**, *142*, 1465–1474.

(21) Ohkita, H.; Cook, S.; Astuti, Y.; Duffy, W.; Tierney, S.; Zhang, W.; Heeney, M.; McCulloch, I.; Nelson, J.; Bradley, D. D.; Durrant, J. R. Charge Carrier Formation in

Polythiophene/Fullerene Blend Films Studied by Transient Absorption Spectroscopy. *J. Am. Chem. Soc.* **2008**, *130*, 3030–3042.

(22) Gregg, B. A. Entropy of Charge Separation in Organic Photovoltaic Cells: The Benefit of Higher Dimensionality. *J. Phys. Chem. Lett.* **2011**, *2*, 3013–3015.

(23) Guo, J.; Ohkita, H.; Benten, H.; Ito, S. Charge Generation and Recombination Dynamics in Poly(3-hexylthiophene)/Fullerene Blend Films with Different Regioregularities and Morphologies. *J. Am. Chem. Soc.* **2010**, *132*, 6154–6164.

(24) Groves, C. Developing Understanding of Organic Photovoltaic Devices: Kinetic Monte Carlo Models of Geminate and Non-Geminate Recombination, Charge Transport and Charge Extraction. *Energy Environ. Sci.* **2013**, *6*, 3202–3217.

(25) Natsuda, S.; Saito, T.; Shirouchi, R.; Sakamoto, Y.; Takeyama, T.; Tamai, Y.; Ohkita, H. Cascaded Energy Landscape as a Key Driver for Slow Yet Efficient Charge Separation with Small Energy Offset in Organic Solar Cells. *Energy Environ. Scie.* **2022**, *15*, 1545–1555.

(26) Zhang, G. et al. Delocalization of Exciton and Electron Wavefunction in Non-Fullerene Acceptor Molecules Enables Efficient Organic Solar Cells. *Nat. Commun,* **2020**, *11*, 3943.

(27) Bartynski, A. N.; Gruber, M.; Das, S.; Rangan, S.; Mollinger, S.; Trinh, C.; Bradforth, S. E.; Vandewal, K.; Salleo, A.; Bartynski, R. A.; Bruetting, W.; Thompson, M. E. Symmetry-Breaking Charge Transfer in a Zinc Chlorodipyrrin Acceptor for High Open Circuit Voltage Organic Photovoltaics. *J. Am. Chem. Soc.* **2015**, *137*, 5397–5405.

(28) Ramirez, C. E.; Chen, S.; Powers-Riggs, N. E.; Schlesinger, I.; Young, R. M.; Wasielewski, M. R. Symmetry-Breaking Charge Separation in the Solid State: Tetra(phenoxy)perylenediimide Polycrystalline Films. *J. Am. Chem. Soc.* **2020**, *142*, 18243–18250.

(29) Sebastian, E.; Hariharan, M. Symmetry-Breaking Charge Separation in Molecular Constructs for Efficient Light Energy Conversion. *ACS Energy Lett.* **2022**, *7*, 696–711.

(30) Wasielewski, M. R. Self-Assembly Strategies for Integrating Light Harvesting and Charge Separation in Artificial Photosynthetic Systems. *Acc. Chem. Res.* **2009**, *42*, 1910–1921.

(31) Vauthey, E. Photoinduced Symmetry-Breaking Charge Separation. *ChemPhysChem.* **2012**, *13*, 2001–2011.

(32) Cook, R. E.; Phelan, B. T.; Kamire, R. J.; Majewski, M. B.; Young, R. M.; Wasielewski, M. R. Excimer Formation and Symmetry-Breaking Charge Transfer in Cofacial Perylene Dimers. *J. Phys. Chem. A* **2017**, *121*, 1607–1615.

(33) Young, R. M.; Wasielewski, M. R. Mixed Electronic States in Molecular Dimers: Connecting Singlet Fission, Excimer Formation, and Symmetry-Breaking Charge Transfer. *Acc. Chem. Res.* **2020**, *53*, 1957–1968.

(34) Azumi, T.; McGlynn, S. Energy of Excimer Luminescence. I. A Reconsideration of Excimer Processes. *J. Chem. Phys.* **1964**, *41*, 3131–3138.

(35) Azumi, T.; Armstrong, A. T.; McGlynn, S. Energy of Excimer Luminescence. II. Configuration Interaction between Molecular Exciton States and Charge Resonance States. *J. Chem. Phys.* **1964**, *41*, 3839–3852.

(36) Azumi, T.; McGlynn, S. Energy of Excimer Luminescence. III. Group Theoretical Considerations of Molecular Exciton and Charge Resonance States. *J. Chem. Phys.* **1965**, *42*, 1675–1680.

(37) Birks, J. Excimers. *Rep. Prog. Phys.* **1975**, *38*, 903.

(38) Ota, W.; Takahashi, K.; Higashiguchi, K.; Matsuda, K.; Sato, T. Origin of Aggregation-Induced Enhanced Emission: Role of Pseudo-Degenerate Electronic States of Excimers Formed in Aggregation Phases. *J. Mater. Chem. C* **2020**, *8*, 8036–8046.

(39) Bersuker, I. B.; Polinger, V. Z. *Vibronic Interactions in Molecules and Crystals*; Springer-Verlag: Berlin and Heidelberg, 1989.

(40) Bersuker, I. B. Pseudo-Jahn–Teller Effect: A Two-State Paradigm in Formation, Deformation, and Transformation of Molecular Systems and Solids. *Chem. Rev.* **2013**, *113*, 1351–1390.

(41) Sato, T.; Tokunaga, K.; Tanaka, K. Vibronic Coupling in Naphthalene Anion: Vibronic Coupling Density Analysis for Totally Symmetric Vibrational Modes. *J. Phys. Chem. A* **2008**, *112*, 758–767.

(42) Uejima, M.; Sato, T.; Yokoyama, D.; Tanaka, K.; Park, J.-W. Quantum Yield in Blue-Emitting Anthracene Derivatives: Vibronic Coupling Density and Transition Dipole Moment Density. *Phys. Chem. Chem. Phys.* **2014**, *16*, 14244–14256.

(43) Kato, K.; Haruta, N.; Sato, T. *Vibronic Coupling Density : Understanding Molecular Deformation*; Springer: Singapore, 2021.

(44) Umeyama, T.; Igarashi, K.; Tamai, Y.; Wada, T.; Takeyama, T.; Sasada, D.; Ishida, K.; Koganezawa, T.; Ohtani, S.; Tanaka, K.; Ohkita, H.; Imahori, H. Prolongation of the Singlet Exciton Lifetime of Nonfullerene Acceptor Films by the Replacement of the Central Benzene Core with Naphthalene. *Sustain. Energy Fuels* **2021**, *5*, 2028–2035.

(45) Fischer, G. *Vibronic Coupling: The Interaction between the Electronic and Nuclear Motions*; Academic Press: London, 1984.

(46) Azumi, T.; Matsuzaki, K. What Does the Term ”Vibronic Coupling” Mean? *Photochem. Photobiol.* **1977**, *25*, 315–326.

(47) Bersuker, I. On the Origin of Ferroelectricity in Perovskite-Type Crystals. *Phys. Lett.* **1966**, *20*, 589–590.

(48) Polinger, V.; Garcia-Fernandez, P.; Bersuker, I. Pseudo Jahn–Teller Origin of Ferroelectric Instability in $BaTiO_3$ Type Perovskites: The Green's Function Approach and Beyond. *Phys. B: Condens. Matter* **2015**, *457*, 296–309.

(49) Sato, T.; Uejima, M.; Tanaka, K.; Kaji, H.; Adachi, C. A Light-Emitting Mechanism for Organic Light-Emitting Diodes: Molecular Design for Inverted Singlet–Triplet Structure and Symmetry-Controlled Thermally Activated Delayed Fluorescence. *J. Mater. Chem. C* **2015**, *3*, 870–878.

(50) Tomasi, J.; Mennucci, B.; Cammi, R. Quantum Mechanical Continuum Solvation Models. *Chem. Rev.* **2005**, *105*, 2999–3094.

(51) Frisch, M. J. et al. Gaussian 16 Revision A.03. 2016; Gaussian Inc. Wallingford CT.

(52) Han, G.; Guo, Y.; Song, X.; Wang, Y.; Yi, Y. Terminal π–π Stacking Determines Three-Dimensional Molecular Packing and Isotropic Charge Transport in an A–π–A Electron Acceptor for Non-Fullerene Organic Solar Cells. *J. Mater. Chem. C* **2017**, *5*, 4852–4857.

(53) Aldrich, T. J.; Matta, M.; Zhu, W.; Swick, S. M.; Stern, C. L.; Schatz, G. C.; Facchetti, A.; Melkonyan, F. S.; Marks, T. J. Fluorination Effects on Indacenodithienothiophene Acceptor Packing and Electronic Structure, End-Group Redistribution, and Solar Cell Photovoltaic Response. *J. Am. Chem. Soc.* **2019**, *141*, 3274–3287.

(54) Li, D.; Zhang, X.; Liu, D.; Wang, T. Aggregation of Non-Fullerene Acceptors in Organic Solar Cells. *J. Mater. Chem. A* **2020**, *8*, 15607–15619.

(55) Sato, T.; Hayashi, R.; Haruta, N.; Pu, Y.-J. Fluorescence via Reverse Intersystem

Crossing from Higher Triplet States in a Bisanthracene Derivative. *Sci. Rep.* **2017**, *7*, 4820.

(56) Goto, H.; Obata, S.; Nakayama, N.; Ohta, K. CONFLEX 9. 2021; CONFLEX Corporation, Tokyo, Japan.

(57) Chung, L. W.; Sameera, W.; Ramozzi, R.; Page, A. J.; Hatanaka, M.; Petrova, G. P.; Harris, T. V.; Li, X.; Ke, Z.; Liu, F.; Li, H.-B.; Ding, L.; Morokuma, K. The ONIOM Method and Its Applications. *Chem. Rev.* **2015**, *115*, 5678–5796.

TOC Graphic

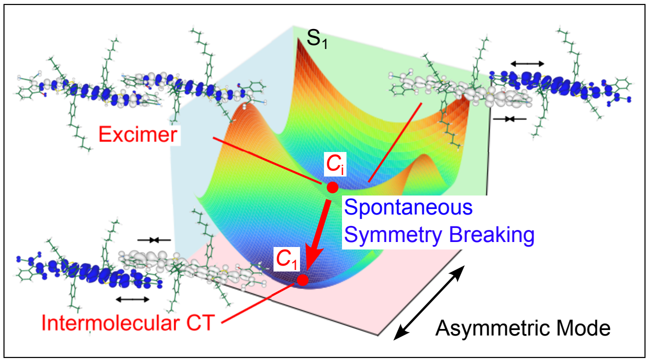
S$_1$
Excimer
C_i
Spontaneous Symmetry Breaking
C_1
Intermolecular CT
Asymmetric Mode